Monoliths of Semiconducting Block Copolymers by Magnetic Alignment

Helen Tran,[†,§] Manesh Gopinadhan,[‡,§] Pawel W. Majewski,[‡,§] Ryan Shade,[†] Victoria Steffes,[†] Chinedum O. Osuji,[‡,*] and Luis M. Campos[†,*]

[†]Department of Chemistry, Columbia University, New York, New York 10027, United States, and [‡]Department of Chemical and Environmental Engineering, Yale University, New Haven, Connecticut 06511, United States. [§]H. Tran, M. Gopinadhan, and P. W. Majewski contributed equally to this work.

ABSTRACT Achieving highly ordered and aligned assemblies of organic semiconductors is a persistent challenge for improving the performance of organic electronics. This is an acute problem in macromolecular systems where slow kinetics and long-range disorder prevail, thus making the fabrication of high-performance large-area semiconducting polymer films a nontrivial venture. Here, we demonstrate that the anisotropic nature of semiconducting chromophores can be effectively leveraged to yield hierarchically ordered materials that can be readily macroscopically aligned. An n-type mesogen was synthesized based on a perylene diimide (PDI) rigid core coupled to an imidazole headgroup *via* an alkyl spacer. Supramolecular assembly between the imidazole and acrylic acid units on a poly(styrene-*b*-acrylic acid) block copolymer yielded self-assembled hexagonally ordered polystyrene cylinders within a smectic A mesophase of the PDI mesogen and poly(acrylic acid). We show that magnetic fields can be used to control the alignment of the PDI species and the block copolymer superstructure concurrently in a facile manner during cooling from a high-temperature disordered state. The resulting materials are monoliths, with a single well-defined orientation of the semiconducting chromophore and block copolymer microdomains throughout the sample. This synergistic introduction of both functional properties and the means of controlling alignment by supramolecular attachment of mesogenic species to polymer backbones offer new possibilities for the modular design of functional nanostructured materials.

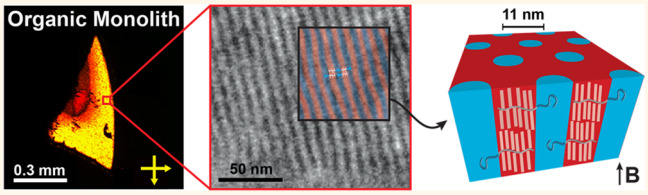

KEYWORDS: n-type semiconductors · magnetic-field alignment · organic monoliths · block copolymer self-assembly

Organic electronic materials have enabled a wide range of new technologies since they were discovered to conduct charge.[1−4] Prime examples include the development of electronic paper, commercially available organic light emitting diode displays, and plastic solar cells, among other devices.[5−7] To date, the most widely studied organic electronic materials fall within two categories, small molecules and linear backbone conjugated polymers.[8−10] Small molecules generally exhibit higher mobilities than their macromolecular counterparts, in part due to their crystallinity. Conjugated polymers are generally attractive for their solution processability as opposed to the vapor processes typically employed for small molecules. Recently, high mobilities have been reported in several semiconducting polymers.[11−14] However, grain boundaries between crystalline domains, as well as amorphous−crystalline interfaces, dwarf performance by providing charge-trapping sites.[15] Additionally, it is imperative to control the alignment of the crystalline domains in the direction of the crystallographic axis that leads to the highest charge carrier mobility in a device. Current processing methods do not permit such control of orientation in a simple manner, and organic materials generally yield system-specific results.[16] The development of an effective generalized strategy to control ordering and alignment of organic semiconductors over large areas is thus necessary.

The use of liquid crystalline (LC) organization of semiconducting moieties is promising, given the general susceptibility of LC mesophases to orientational control by external stimuli. Several small-molecule systems have demonstrated attractive electronic properties,[17,18] but suffer from relatively fast relaxation dynamics of the mesogens, which can disrupt the transport properties. Further, the ordered mesophases can be sensitive to fluctuations in the environment, for example, temperature and external fields. Polymer LCs exhibit slower dynamics in comparison to small-molecule LCs. In an elegant approach, semiconducting LC polymers, including block

* Address correspondence to lcampos@columbia.edu, chinedum.osuji@yale.edu.

Received for review April 8, 2013 and accepted May 14, 2013.

Published online May 20, 2013
10.1021/nn401725a

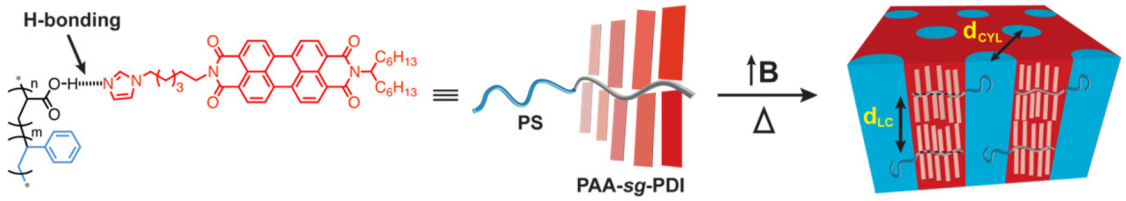

Figure 1. Illustration of the use of PS-b-PAA as a template to magnetically induce the alignment of the perylene diimide (PDI) mesogens upon thermal annealing. "B" is the magnetic field, and supramolecular graft is abbreviated as "*sg*".

copolymers (BCPs), have been realized by side-chain attachment of semiconducting mesogens to the polymer backbone.[19−22] A particularly compelling aspect is the ability to combine BCP self-assembly with the selective attachment of p- and n-type semiconducting mesogens on the polymer backbone. Self-organization of the mesogens within the BCP superstructure produces a hierarchically ordered system in which the semiconducting moieties are effectively sequestered in nanometer-scale domains. While the confinement of the mesogens by the BCP domains tends to improve mesophase order and restrict unwanted reorganization, the presence of grain boundaries in the BCP structure and the tortuosity of BCP domains present obstacles to realizing the so needed macroscopically ordered and aligned channels of semiconducting materials.[23] We are therefore faced with the challenge to control the alignment of the BCP by manipulating the alignment of the semiconducting species within the BCP domains.

Here, stimuli-responsive materials were designed to explore a facile, nondestructive, large-scale technique using a magnetic field to align semiconducting side-chain BCPs at the nanoscale (Figure 1). The supramolecular system comprises a polystyrene-*b*-poly(acrylic acid) (PS-*b*-PAA) backbone to which an imidazole-functional perylene diimide (PDI) mesogen is attached by hydrogen bonding with the PAA block. PDI serves as an attractive, model n-type semiconductor since it can be asymmetrically functionalized and it is a flat, rigid molecule.[24,25] The dynamic nature of the hydrogen bond combined with the presence of an alkyl spacer serves to sufficiently decouple the mesogen from the polymer backbone,[26] enabling the formation of a smectic mesophase within the system. The molecular mass and composition of the BCPs were varied in order to study the effects on the morphology upon cooling from a high-temperature disordered state under an applied magnetic field. This results in the formation of organic monoliths within which the long axis of the semiconducting mesogens and BCP domains are aligned parallel to the field direction throughout the material (Figure 1). This method is particularly attractive due to its scalability. Further, the supramolecular grafting strategy provides modularity, as it allows for the facile utilization of different semiconducting mesogens and the variation of their stoichiometry to successfully obtain field-responsive liquid crystalline semiconducting BCPs.

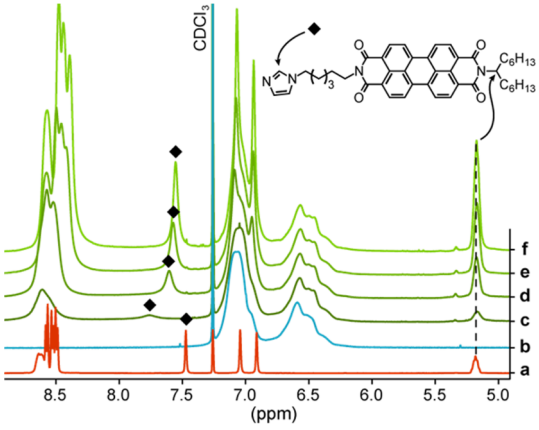

Figure 2. ^{1}H NMR spectra (field range omits the aliphatic region) of (a) PDI mesogen only, (b) PS(5.2k)-*b*-PAA(4k) only, and PS(5.2k)-*b*-[PAA(4k)-*sg*-PDI] at *R* = (c) 0.25, (d) 0.5, (e) 0.75, and (f) 1.0 in $CDCl_3$. The aromatic proton that shifts upon hydrogen bonding is labeled with a diamond symbol in the spectra and the chemical structure. The tertiary hydrogen does not shift upon hydrogen bonding.

RESULTS AND DISCUSSION

To probe the supramolecular interaction between the PS-*b*-PAA BCP and PDI mesogens, we investigated the association of the PDI mesogens in solution by proton nuclear magnetic resonance spectroscopy (^{1}H NMR, Figure 2) and in the solid-state by Fourier transform infrared spectroscopy (FTIR; see Supporting Information [SI] Figure S1). The ^{1}H NMR spectra of neat PS(5.2k)-*b*-PAA(4k), PDI mesogens, and their mixtures PS(5.2k)-*b*-[PAA(4k)-*sg*-PDI] (where *sg* = supramolecular graft, and the values in parentheses are the molecular mass of the blocks) at various molar ratios *R* in deuterated chloroform ($CDCl_3$) are shown in Figure 2 (*R* = moles of PDI relative to the AA units). Peak broadening of the aromatic perylene hydrogens is exhibited at all *R* values, evident of PDI mesogen association to the polymer backbone. Upon hydrogen bonding, the proton signal from the 2-position of the imidazole ring clearly shifts downfield, from *ca.* 7.45 ppm to 7.75 ppm, at *R* = 0.25. The peak moves upfield with increasing *R* of the PDI mesogen, and a characteristic broadening of the mesogenic proton peaks is observed, consistent with the incorporation of the PDI into the polymer and slowing of the

rotational dynamics of the species. We speculate that there is more free mesogen at larger R values, as indicated by the peak sharpening for $R > 0.75$, which may be driven by steric crowding and chain stretching along the PAA backbone at such high loading. The corresponding ^{1}H NMR spectra in deuterated tetrahydrofuran (THF-d_8) displayed similar trends (SI, Figure S2). To corroborate hydrogen bonding in the solid state, the characteristic carbonyl absorption bands in the 1750−1680 cm^{-1} region were monitored by IR (SI, Figure S1) as a function of R in the solid state. We observe a steady shift of the carbonyl band with increasing R, which is indicative of hydrogen bonding between the imidazole and acrylic acid units, as previously reported.[27]

The NMR data indicate that working with incorporation of one PDI mesogen to two or three AA repeat units ($R = 0.50$ or 0.33, respectively) would not lead to a highly crowded backbone. Differential scanning calorimetry (DSC) traces of bulk samples prepared from neat and mixed solutions of PS(5.2k)-*b*-PAA(4k) and PDI mesogens showed clear evidence of the formation of a supramolecular complex, as revealed by the distinct thermal transitions of the mixed materials relative to their pure states (SI, Figure S3). For $R = 0.33$ and 0.5, endothermic peaks at 190 and 210 °C correspond to the liquid crystal clearing temperature, T_{iso}. Drop-cast bulk samples exhibit BCP microphase segregation and the formation of randomly oriented domains, as evidenced from small-angle X-ray scattering (SAXS, Figure S4). The system shows two scattering maxima, at $q = 0.056$ Å^{-1} and $q = 0.113$ Å^{-1}, corresponding to d-spacing values ($d = 2\pi/q$) of 11.2 and 5.5 nm. The reflection at $q = 0.113$ Å^{-1} is due to the LC mesophase formed by the PDI mesogen, whereas the peak at smaller q (0.056 Å^{-1}) originates from the BCP microphase segregated structure. The mass fraction of PS in the sample is roughly 0.18, which suggests that the system should form hexagonally packed PS cylinders, assuming roughly similar mass densities of the PS and PAA-*sg*-PDI matrix. The absence of higher order peaks of the primary scattering, however, did not permit unambiguous assignment of the microstructure. By comparison, neat PS(5.2k)-*b*-PAA(4k) forms a well-ordered lamellar morphology with a d-spacing of 18.2 nm (SI, Figure S4). The lamellar morphology is expected because the volume fraction of PS in this strongly segregated system is 57%. The decrease of the d-spacing upon addition of PDI mesogens, despite the increase in the mass of the system, suggests that the PDI mesogens significantly decrease the interaction parameter between the PS and PAA backbones. Similar effects have been observed for biphenyl mesogens in PS-*b*-PAA.[28]

To test the hypothesis highlighted in Figure 1, a sample containing PS(5.2k)-*b*-[PAA(4k)-*sg*-PDI] at $R = 0.50$ was heated to 215 °C, which is above the highest clearing temperature found from DSC. The sample was equilibrated at this temperature for 5 min and then cooled to 25 °C in the presence of the magnetic field (6 T) at 1 °C/min. The sample was microtomed and stained to obtain cross-sectional transmission electron microscopy (TEM) images of the magnetically annealed bulk material. Figure 3 shows the morphology of the nanostructured monolith, composed of hexagonally packed PS cylinders (bright regions) aligned in the direction of the field and embedded in a PAA-*sg*-PDI matrix. The 6-fold symmetry of the Fourier transform (FFT), along the field direction, is consistent with a hexagonally packed cylindrical microphase separated structure, in agreement with the estimated volume fraction of the system (inset, Figure 3a and SI, Table S1).

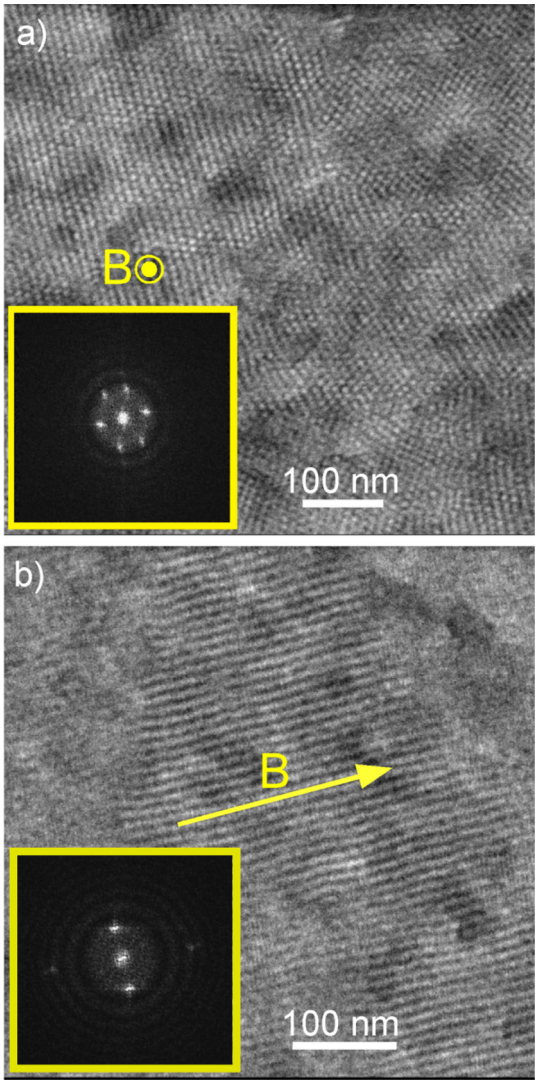

Figure 3. Cross-sectional TEM images of PS(5.2k)-*b*-[PAA(4k)-*sg*-PDI] at $R = 0.5$. Hexagonally packed PS cylinders (bright regions) surrounded by PAA and PDI matrix are imaged (a) orthogonal to and (b) along the magnetic field of direction with corresponding Fourier transforms over the entire micrograph (insets). The Fourier transforms indicate 6- or 2-fold symmetry in the morphology, depending on the field direction. The reflection orthogonal to the BCP structure arises from the smectic layers.

In the direction orthogonal to the magnetic field, the TEM image shows PS cylinders parallel to the applied magnetic field and the expected 2-fold symmetry for this projection from the FFT (Figure 3b). Notably, the matrix surrounding the PS cylinders shows alignment of the smectic layers of PDI perpendicular to the field direction; that is, the director of the mesophase is parallel to the field, as are the long axes of the PDI mesogens. The TEM data unequivocally demonstrate that the schematic of Figure 1 is descriptive of the organization of the system for R = 0.50 as well as R = 0.33 (SI, Figure S5).

In order to extract detailed structural information about the evolution of the observed morphology, temperature-resolved scattering was used to examine the proximity of T_{ODT} and T_{iso}, in the absence and presence of the field (Figure 4 and SI, Figure S6).

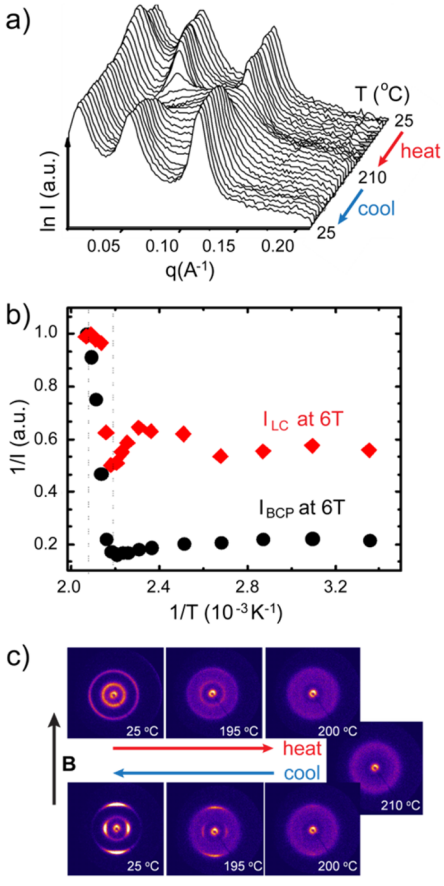

Figure 4. (a) Temperature-resolved SAXS data of PS(5.2k)-*b*-[PAA(4k)-*sg*-PDI] with R = 0.5 with the presence of a magnetic field. 1D integrated data show two prominent intensities at q = 0.056 Å^{-1} (d = 11.2 nm) and q = 0.113 Å^{-1} (d = 5.5 nm). (b) Normalized inverse peak intensities of microdomains and smectic scattering, represented as a function of inverse temperature to indicate overlap of T_{ODT} and clearing transition T_{iso}. (c) Characteristic diffraction rings from the disorganized PS cylinders and PDI smectic layers diminish when heated above the order−disorder transition temperature, T_{ODT}. Upon cooling in the presence of a magnetic field though T_{ODT}, anisotropic rings reflecting the orientation of aligned morphologies reappear, as shown in the 2D SAXS patterns.

At 25 °C, two prominent peaks are present, originating from the periodic arrangement of BCP microdomains (q_{BCP} = 0.056 Å^{-1}; d_{BCP} = 11.2 nm) and PDI mesogens (q_{LC} = 0.113 Å^{-1}; d_{LC} = 5.5 nm). The distance between cylinders is $d_{CYL} = (4/3)^{1/2}$ and d_{BCP} = 12.9 nm. The intensities of both peaks diminish simultaneously with increasing temperature until there is only a broad hump centered near q = 0.10 Å^{-1} at temperatures above *ca.* 200 °C. The absence of both peaks above this temperature indicates that the LC mesophase is above its clearing temperature, T_{iso}, and that the BCP is also above its T_{ODT}. The overlap between these two transitions is clear from the 1/I(1/T) plot (Figure 4b), indicating that this system is weakly segregated, independent of the presence of the field. A sigmoidal fit of the data yielded $T_{ODT} \approx T_{iso} \approx$ 200 °C. The small discrepancy between T_{iso} derived from scattering and that from DSC is likely due only to a built-in offset between the DSC and the custom-built SAXS heating stage. Upon cooling to 25 °C, both peaks re-emerge with marginal undercooling below 200 °C as the system orders on the BCP and LC length scales. While the magnetic field does not influence the location of phase transitions in any measurable manner, the influence on the morphology is striking, as shown in the temperature-resolved 2D SAXS data measured during heating and cooling under a 6 T field (Figure 4c). The data show strong anisotropy for both the BCP and LC scattering on cooling from 200 °C. The periodicity of the BCP domains is orthogonal to the field, while the 5.5 nm periodicity of the LC mesophase is parallel to the field. This is consistent with alignment of the cylindrical microdomains along the field direction, with smectic layers of the PDI mesogen also aligned normal to the field. This suggests that the mesogens display positive magnetic anisotropy, resulting in alignment parallel to the interface between the two blocks, *i.e.*, exhibiting a planar or homogeneous anchoring condition, and assembled as a smectic A mesophase.

The high degree of alignment achieved here is remarkable and likely due in part to the small separation of T_{iso} and T_{ODT}. Prior work has established that field alignment of LC BCPs is most effective when the isotropic transition of the LC, T_{iso}, is in close proximity to the order−disorder transition of the block copolymer, T_{ODT},[29] as common in weakly segregated systems.[30] Under these circumstances, cooling the sample from the high-temperature disordered state in the presence of the field results in a maximal coupling of the high, but rapidly decreasing, mobility and the small, but rapidly increasing, magnetic anisotropy of both incipient ordered states.[31] This is in contrast to a scenario where $T_{ODT} > T_{iso}$, in which case the alignment can be poor since it occurs as the LC mesophase develops within a pre-existing low-mobility ordered state of the BCP.

We examined mesogen ordering within the smectic layers using wide-angle X-ray scattering (WAXS), which

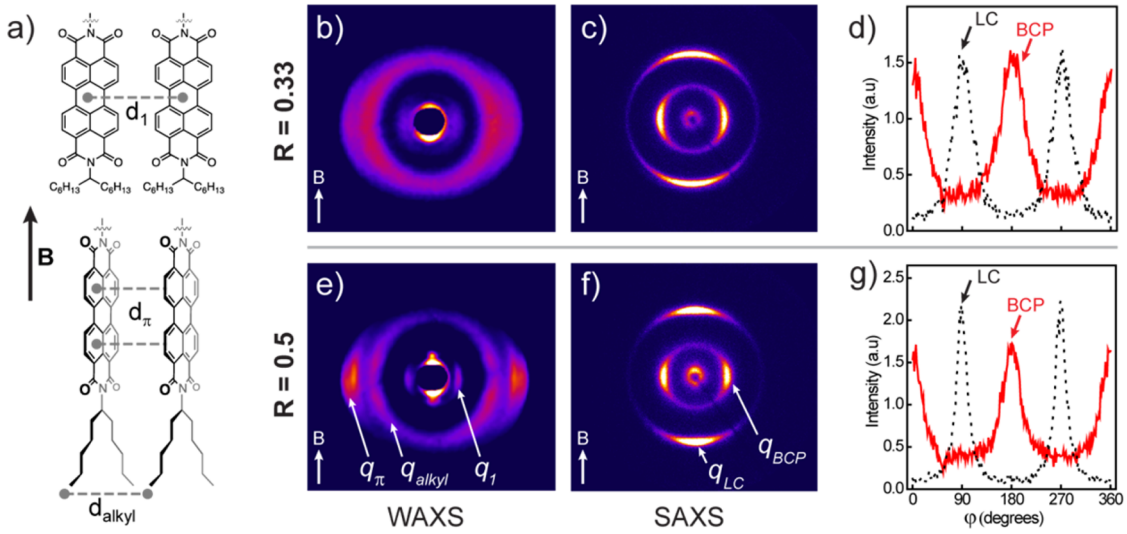

Figure 5. (a) Schematic representation of the corresponding labels shown in the 2D WAXS plots, along with the direction of the magnetic field, *B*. Room-temperature 2D WAXS (b) and SAXS (c) data for PS(5.2k)-*b*-[PAA(4k)-*sg*-PDI] at $R = 0.33$ after magnetic alignment at 6 T. (d) Azimuthal dependence of scattered intensity for LC and BCP primary peaks for $R = 0.33$. Room-temperature 2D WAXS (e) and SAXS (f) data for PS(5.2k)-*b*-[PAA(4k)-*sg*-PDI] at $R = 0.50$ after magnetic alignment at 6 T. (g) Azimuthal dependence of scattered intensity for LC and BCP primary peaks for $R = 0.50$. The magnetic field direction was vertical with respect to the diffractograms. The degenerate orientation of the PDI mesogen core relative to the magnetic field results in reflections at $q_\pi = 1.82$ Å^{-1} corresponding to a $\pi-\pi$ stacking distance of 3.45 Å and at $q_1 = 0.63$ Å^{-1} ($d_1 = 10$ Å) due to the lateral distance between PDI mesogens. Tilt of the alkyl tails results in symmetric reflections at $q_{alkyl} = 1.43$ Å^{-1} ($d_{alkyl} = 4.4$ Å).

yielded information on $\pi-\pi$ stacking distances and alignment of the mesogens relative to the magnetic field (Figure 5a). A $\pi-\pi$ stacking distance of $d_\pi = 3.45$ Å ($q_\pi = 1.82$ Å^{-1}) and lateral periodicity between mesogens (along their edges) of $d_1 = 10$ Å ($q_1 = 0.63$ Å^{-1}) were obtained (Figure 5b and e). The strict orthogonality between the SAXS reflection with a *d*-spacing of 5.5 nm (visible near the center of the WAXS data, Figure 5b and e, and in SAXS, Figure 5c and f) and both the $\pi-\pi$ stacking and lateral periodicity indicate unambiguously that the PDI mesogens form a smectic A mesophase. A 4-fold symmetric peak at $q_{alkyl} = 1.43$ Å^{-1} ($d_{alkyl} = 4.4$ Å) is attributed to tilted packing of the gemini hexyl tails of the mesogen. The concentration of the scattering originating from $\pi-\pi$ stacking and lateral periodicity of the PDI mesogens along the equatorial direction indicates that the long axis of the PDI mesogens is aligned parallel to the field. This implies that these species possess a positive magnetic anisotropy, $\Delta\chi = \chi_{\parallel} - \chi_{\perp}$, resulting in alignment of the molecular long axis along the field with degeneracy of the orientation of the molecule in the plane perpendicular to the field.

The aziumuthal dependence of the scattered intensity provides a quantitative measure of the degree of alignment of the smectic mesophase of the PDI mesogen and the cylindrical microdomains of the BCP (Figure 5d and g). For $R = 0.5$, the full-widths at half-maximum (fwhm) for the BCP and LC peaks are 39° and 23°, respectively, whereas for $R = 0.33$ the corresponding fwhm are 53° and 40°. Using a Gaussian approximation for the intensity distribution we can correlate the fwhm with the scalar coefficient of the orientation distribution function for uniaxial symmetry, $P_2 = (1/2)(3\cos^2\theta - 1)$; that is, we can estimate the orientational order parameter *S* by evaluating the average of this second Legendre polynomial, as shown in eq 1.

$$S = \langle P_2(\cos\theta)\rangle = \frac{\int_0^{\pi/2} \frac{1}{2}(3\cos^2\theta - 1)\sin\theta\, d\theta}{\int_0^{\pi/2} \sin\theta\, d\theta} \quad (1)$$

Perfectly aligned structures have $S = 1$, while the completely random case corresponds to $S = 0$. We find $S_{LC} = 0.91$ and $S_{BCP} = 0.78$ for $R = 0.5$ and slightly lower values for $R = 0.3$, where $S_{LC} = 0.77$ and $S_{BCP} = 0.64$. These values indicate that the system exhibits a high degree of orientational order. The observation that $S_{LC} > S_{BCP}$ is consistent with the hypothesis that the alignment of the LC mesophase drives the alignment of the BCP, and so S_{LC} places an upper bound on S_{BCP}. Finally, these values compare favorably with prior work on shear alignment of electrostatic PDI complexes[32] and benzoperylene moieties,[33] where dichroic ratios of 18 and 14.3 were observed, respectively. These dichroic ratios correspond to orientational order parameters $S = 0.85$ and $S = 0.82$, where *S* can be related to the dichroic ratio approximately as eq 2.[34]

$$S = \frac{3}{2}\frac{D}{D+2} - \frac{1}{2} = \frac{D-1}{D+2} \quad (2)$$

The highly ordered structures characterized by TEM, SAXS, and WAXS extend continuously throughout all samples studied, with a singular orientation, akin to ceramic monoliths.[35−37] We used polarized optical microscopy to provide a meaningful large-area observation of

TABLE 1. Summary of PS-*b*-PAA Composition and T_{ODT}

total M_n[a] (g/mol)	PS M_n[a] (g/mol)	PAA M_n[a] (g/mol)	wt % PAA	T_{ODT}[b] (°C)
9200	5200	4000	43	195
13 500	7500	6000	44	200
29 700	17 900	11 800	40	230
27 100	20 800	6300	23	240

[a] Determined by size exclusion chromatography (SEC). [b] Determined by temperature-resolved SAXS at $R = 0.4$, except for the parent diblock with $M_n = 9200$ g/mol where $R = 0.50$.

TABLE 2. Summary of *d*-Spacings for Annealed Samples

polymer[a]	d_{BCP} (nm)	d_{LC} (nm)
PS(5.2k)-*b*-PAA(4k)	11.2	5.5
PS(7.5k)-*b*-PAA(6k)	23.0	4.9
PS(17.9k)-*b*-PAA(11.8k)	28.2	5.0
PS(20.8k)-*b*-PAA(6.3k)[b]	26.9	5.3

[a] Determined from 1D SAXS of annealed bulk samples at $R = 0.4$. [b] Unlike the other three polymers, PS(20.8k)-*b*-PAA(6.3k) did not exhibit magnetic alignment.

alignment uniformity through the birefringence of the samples, which originates due to the LC organization of the PDI mesogens (SI, Figure S7). Strong optical birefringence was observed, with uniform extinction of light transmission across a film of millimeter length scale when the field direction used during alignment was parallel to either the polarizer or analyzer. Likewise, the film was uniformly bright when the field, and thus the LC director, was at 45° to the polarizers.

We further demonstrated the ability to tune the domain size of these materials by varying the molecular mass and composition of the polymer backbone. A series of PS-*b*-PAA BCPs was synthesized with characteristics as detailed in Table 1. Two polymers with larger molecular mass, but similar composition to the PS(5.2k)-*b*-PAA(4k) parent polymer, served to investigate the dependence of T_{ODT} on molecular mass. As expected, T_{ODT} increases with total molecular mass for identical molar ratios, as reasoned by the increase of polymer viscosity due to chain entanglement (Table 1). Magnetic alignment of both the 13.5k and 29.7k PS-*b*-[PAA-*sg*-PDI] at $R = 0.4$ using the previously applied cooling rate of 1 °C/min but at higher starting temperature was effective in producing well-aligned samples, without encountering strong kinetic limitations due to the increased molecular mass (SI, Figures S8 and S9). Similar to the 9.2k PS-*b*-[PAA-*sg*-PDI] at $R = 0.4$, both the 13.5k and 29.7k PS-*b*-[PAA-*sg*-PDI] at $R = 0.4$ exhibited a cylindrical morphology. For larger molecular mass BCPs, solvent annealing stands as an attractive alternative to achieve the isotropic state, especially due to thermal degradation of the polymers and side reactions, such as anhydride formation of PAA. The *d*-spacing values obtained with the higher molecular mass systems are given in Table 2. The sharp increase in the *d*-spacing reflects the effect of the increased molecular mass and higher segregation strength between the blocks at the slightly reduced molar ratio ($R = 0.4$). In contrast to these near-symmetric diblocks, a 27.1k PS(20.8k)-*b*-[PAA(6.3k)-*sg*-PDI] with minority PAA block (23 wt %) did not exhibit field alignment for $R = 0.4$ and 0.8 (SI, Figure S10). This may be explained by the fact that for both ratios, T_{ODT} was at least 20 °C higher than T_{iso}, likely due to the lower mass content of the PDI and thus stronger segregation between the blocks. As a result, this system is challenged by the kinetic constraint of aligning in the high-viscosity ordered state of the BCP on crossing T_{iso}.

CONCLUSION

The magnetic alignment of PS-*b*-PAA containing supramolecularly grafted semiconducting PDI mesogens into an organic monolith has been achieved and characterized using a combination of X-ray scattering, NMR, DSC, IR, and TEM characterization techniques. The microstructure of the system is tunable by controlling the polymer molecular mass, composition, and stoichiometry of the mesogen attachment to the acrylic acid units. For the particular compositions studied here, the system exhibited hexagonally packed PS cylinders embedded in a matrix of well-ordered smectic layers of PDI mesogens bound to the PAA block. Alignment was conducted in a facile manner by cooling the system from its high-temperature disordered state in the presence of the magnetic field. The resulting materials display a single orientation of the microstructure throughout the sample, with the PS cylinders and the director of the smectic mesophase of the PDI strongly aligned along the field direction. The space pervasive nature of magnetic fields means that limitations on the size of the sample are imposed only by the dimensions of the available high-field magnet. The use of magnetic fields thus holds considerable promise as a scalable means of controlling texture in semiconducting polymers for organic electronic applications. The supramolecular attachment of the semiconducting species offers significant flexibility, as it enables a modular approach to the design of functional materials, which are amenable to large-area processing. Future studies are geared toward device fabrication and characterization of the charge carrier properties of these highly ordered and aligned systems.

METHODS

Synthesis. All reagents were obtained from commercial sources and used without further purification. All reactions were magnetically stirred under argon and monitored by thin-layer chromatography. Detailed synthesis of the PDI mesogen and accompanying NMR spectra are included in the SI.

PS(5.2k)-*b*-PAA(4k) was purchased from Polymer Source and was used as received. All other PS-*b*-PAA polymers were synthesized by reversible addition−fragmentation chain transfer according to reported literature.

Nuclear Magnetic Resonance. All NMR spectra were recorded on a Bruker instrument at 500 MHz at room temperature. Chemical shifts for ^{1}H NMR spectra are reported in parts per million downfield from Me_4Si and were referenced to residual protonated solvent ($CDCl_3$: δ 7.26; THF-d_8: δ 1.72, 3.58). Chemical shifts for ^{13}C NMR spectra are reported in parts per million downfield from Me_4Si and referenced to protonated solvent ($CDCl_3$: δ 77.0). Data are represented as follows: chemical shift (multiplicity [s = singlet, d = doublet, t = triplet, m = multiplet], coupling constants in hertz, integration).

Sample Preparation. Stock solutions of PS-*b*-PAA and PDI mesogens were prepared in DMF at 5 wt %. Based on the stoichiometric ratio (R), appropriate volumes of the PS-*b*-PAA and PDI mesogen stock solutions were mixed at 70 °C and allowed to stir for a minimum of 4 h to ensure homogeneity. Bulk samples were prepared by evaporating the solution in an Eppendorf tube under vacuum at 75 °C until the solvent was completely removed, resulting in a solid red pellet.

Magnetic Alignment. Bulk samples of approximately 2 mm thick and 3 mm in diameter were sandwiched between thin Kapton windows on a home-built temperature-controlled aluminum stage within a superconducting magnet (American Magnetics Inc.) at a flux density of 6 T. The samples were heated above the T_{ODT}, typically around 200 °C, at 10 °C/min, and then allowed to cool at 1 °C/min to room temperature in the presence of the field. Details of the system and its integration with the X-ray scattering instrument are available in a prior report.[29]

Transmission Electron Microscopy. Polymer samples were supported inside the blocks of epoxy resin (SPI-PON 812, SPI Supplies). Thin sections of the aligned samples with thickness in the range of 70−100 nm were obtained by ultramicrotomy using a diamond knife at room temperature. Sections were retrieved on 200 mesh TEM grids after flotation onto water and stained in OsO_4 vapor (which preferentially stains the PAA-*sg*-PDI block) for 30 min prior to imaging. TEM analyses were performed on FEI Tecnai Osiris TEM with an accelerating voltage of 200 kV.

X-ray Scattering. *In situ* SAXS experiments in high magnetic field were performed on a pinhole-collimated Rigaku SMAX3000 instrument configured with Cu Kα radiation (λ = 1.542 Å). The SAXS instrument uses a microsource generator and pinhole collimation to obtain a beam diameter of 1.2 mm at the sample plane and customized to permit inclusion of the high-field magnet to perform *in situ* scattering. The scattering was recorded onto a two-wire area detector with a resolution of 1024 × 1024 pixels placed at a distance of 80 cm from the sample, permitting access to a range of scattering vectors (q) from 0.015 to 0.21 Å^{-1}. The resulting 2D SAXS patterns were calibrated using a silver behenate standard. 2D patterns were integrated azimuthally to provide intensity, I, *versus* q, where $q = 4\pi \sin(\theta)/\lambda$, where 2θ is the scattering angle. WAXS was recorded onto image plates (Fuji), and data were calibrated using a silicon powder (111) diffraction ring with a d-spacing of 3.1355 Å. For the temperature-resolved measurements, samples were subjected to a heating/cooling rate of 2 °C/min and equilibrated for 2 min at each temperature prior to data acquisition. 2D data were rendered using WSxM.[38]

Differential Scanning Calorimetry. DSC was performed on a Q200 instrument (TA-Instruments) under N_2 flow at a heating/cooling rate of 5 °C/min.

FTIR. The melt samples were pressed into KBr pellets, and the IR measurements were conducted with a Bruker Tensor 27 spectrometer at room temperature.

Polarized Optical Microscopy (POM). Birefringent textures of the aligned samples were observed by POM using a Zeiss Axiovert 200 M inverted microscope.

Conflict of Interest: The authors declare no competing financial interest.

Supporting Information Available: Additional ^{1}H NMR, DSC, FTIR, SAXS, TEM, and POM data; 2D SAXS data of BCPs at R = 0.4; schematic for synthesis of PDI mesogen and corresponding ^{1}H NMR of intermediate and product; schematic for synthesis of PS-*b*-PAA polymers. This material is available free of charge *via* the Internet at http://pubs.acs.org.

Acknowledgment. This work was funded in part by the Department of the Army Basic Research Program (W911NH-12-1-0252), and M.G., P.M., and C.O. acknowledge financial support by NSF through DMR-0847534. The use of facilities was supported by YINQE and NSF MRSEC DMR-1119826. H.T. thanks the Department of Defense (DOD) for the National Defense Science & Engineering Graduate (NDSEG) Fellowship. We also thank N. Gupta for initially providing some perylene diimide.

REFERENCES AND NOTES

1. Chiang, C. K.; Fincher, C. R.; Park, Y. W.; Heeger, A. J.; Shirakawa, H.; Louis, E. J.; Gau, S. C.; MacDiarmid, A. G. Electrical Conductivity in Doped Polyacetylene. *Phys. Rev. Lett.* **1977**, *39*, 1098–1101.
2. Heeger, A. J. Semiconducting and Metallic Polymers: The Fourth Generation of Polymeric Materials (Nobel Lecture). *Angew. Chem., Int. Ed.* **2001**, *40*, 2591–2611.
3. MacDiarmid, A. G. "Synthetic Metals": A Novel Role for Organic Polymers (Nobel Lecture). *Angew. Chem., Int. Ed.* **2001**, *40*, 2581–2590.
4. Shirakawa, H. The Discovery of Polyacetylene Film: The Dawning of an Era of Conducting Polymers (Nobel Lecture). *Angew. Chem., Int. Ed.* **2001**, *40*, 2574–2580.
5. Loo, Y.-L.; McCulloch, I. Progress and Challenges in Commercialization of Organic Electronics. *MRS Bull.* **2008**, *33*, 653–662.
6. Sirringhaus, H.; Ando, M. Materials Challenges and Applications of Solution-Processed Organic Field-Effect Transistors. *MRS Bull.* **2008**, *33*, 676–682.
7. Brabec, C. J.; Durrant, J. R. Solution-Processed Organic Solar Cells. *MRS Bull.* **2008**, *33*, 670–675.
8. Bendikov, M.; Wudl, F.; Perepichka, D. F. Tetrathiafulvalenes, Oligoacenenes, and Their Buckminsterfullerene Derivatives: The Brick and Mortar of Organic Electronics. *Chem. Rev.* **2004**, *104*, 4891–4946.
9. Patil, A. O.; Heeger, A. J.; Wudl, F. Optical Properties of Conducting Polymers. *Chem. Rev.* **1988**, *88*, 183–200.
10. Coropceanu, V.; Cornil, J.; da Silva Filho, D. A.; Olivier, Y.; Silbey, R.; Brédas, J.-L. Charge Transport in Organic Semiconductors. *Chem. Rev.* **2007**, *107*, 926–952.
11. Tsao, H. N.; Cho, D. M.; Park, I.; Hansen, M. R.; Mavrinskiy, A.; Yoon, D. Y.; Graf, R.; Pisula, W.; Spiess, H. W.; Müllen, K. Ultrahigh Mobility in Polymer Field-Effect Transistors by Design. *J. Am. Chem. Soc.* **2011**, *133*, 2605–2612.
12. Yan, H.; Chen, Z.; Zheng, Y.; Newman, C.; Quinn, J. R.; Dötz, F.; Kastler, M.; Facchetti, A. A High-Mobility Electron-Transporting Polymer for Printed Transistors. *Nature* **2009**, *457*, 679–686.
13. Fan, J.; Yuen, J. D.; Wang, M.; Seifter, J.; Seo, J.-H.; Mohebbi, A. R.; Zakhidov, D.; Heeger, A.; Wudl, F. High-Performance Ambipolar Transistors and Inverters from an Ultralow Bandgap Polymer. *Adv. Mater.* **2012**, *24*, 2186–2190.
14. Li, J.; Zhao, Y.; Tan, H. S.; Guo, Y.; Di, C.-A.; Yu, G.; Liu, Y.; Lin, M.; Lim, S. H.; Zhou, Y.; *et al.* A Stable Solution-Processed Polymer Semiconductor with Record High-Mobility for Printed Transistors. *Sci. Rep.* **2012**, *2*, 754. Online: http://www.nature.com/srep/2012/121018/srep00754/full/srep00754.html. Accessed 5/20/2013.
15. Sirringhaus, H.; Brown, P. J.; Friend, R. H.; Nielsen, M. M.; Bechgaard, K.; Langeveld-Voss, B. M. W.; Spiering, A. J. H.; Janssen, R. a. J.; Meijer, E. W.; *et al.* Two-Dimensional Charge Transport in Self-organized, High-Mobility Conjugated Polymers. *Nature* **1999**, *401*, 685–688.
16. Anthony, J. E.; Facchetti, A.; Heeney, M.; Marder, S. R.; Zhan, X. n-Type Organic Semiconductors in Organic Electronics. *Adv. Mater.* **2010**, *22*, 3876–3892.
17. Kreouzis, T.; Baldwin, R. J.; Shkunov, M.; McCulloch, I.; Heeney, M.; Zhang, W. High Mobility Ambipolar Charge

Transport in a Cross-linked Reactive Mesogen at Room Temperature. *Appl. Phys. Lett.* **2005**, *87*, 172110.
18. Nielsen, C. B.; Angerhofer, A.; Abboud, K. A.; Reynolds, J. R. Discrete Photopatternable π-Conjugated Oligomers for Electrochromic Devices. *J. Am. Chem. Soc.* **2008**, *130*, 9734–9746.
19. Rancatore, B. J.; Mauldin, C. E.; Tung, S.-H.; Wang, C.; Hexemer, A.; Strzalka, J.; Fréchet, J. M. J.; Xu, T. Nano structured Organic Semiconductors *via* Directed Supramolecular Assembly. *ACS Nano* **2010**, *4*, 2721–2729.
20. Kohn, P.; Ghazaryan, L.; Gupta, G.; Sommer, M.; Wicklein, A.; Thelakkat, M.; Thurn-Albrecht, T. Thermotropic Behavior, Packing, and Thin Film Structure of an Electron Accepting Side-Chain Polymer. *Macromolecules* **2012**, *45*, 5676–5683.
21. Yoon, J.; Jin, S.; Ahn, B.; Rho, Y.; Hirai, T.; Maeda, R.; Hayakawa, T.; Kim, J.; Kim, K.-W.; Ree, M. Phase Transitions in Thin Films of a Diblock Copolymer Composed of a Linear Polymer Block and a Brush Polymer Block with Mesogenic Oligothiophenyl Bristles. *Macromolecules* **2008**, *41*, 8778–8784.
22. Aitken, B. S.; Wieruszewski, P. M.; Graham, K. R.; Reynolds, J. R.; Wagener, K. B. Control of Charge-Carrier Mobility *via* In-Chain Spacer Length Variation in Sequenced Triarylamine Functionalized Polyolefins. *ACS Macro Lett.* **2012**, *1*, 324–327.
23. Treat, N. D.; Campos, L. M.; Dimitriou, M. D.; Ma, B.; Chabinyc, M. L.; Hawker, C. J. Nanostructured Hybrid Solar Cells: Dependence of the Open Circuit Voltage on the Interfacial Composition. *Adv. Mater.* **2010**, *22*, 4982–4986.
24. Würthner, F.; Stolte, M. Naphthalene and Perylene Diimides for Organic Transistors. *Chem. Commun.* **2011**, *47*, 5109–5115.
25. Neuteboom, E. E.; Beckers, E. H. A.; Meskers, S. C. J.; Meijer, E. W.; Janssen, R. A. J. Singlet-Energy Transfer in Quadruple Hydrogen-Bonded Oligo(p-phenylenevinylene)perylene-Diimide Dyads. *Org. Biomol. Chem.* **2003**, *1*, 198–203.
26. Engel, M.; Hisgen, B.; Keller, R.; Kreuder, W.; Reck, B.; Ringsdorf, H.; Schmidt, H.-W.; Tschirner, P. Synthesis, Structure and Properties of Liquid Crystalline Polymers. *Pure Appl. Chem.* **1985**, *57*, 1009–1014.
27. Gopinadhan, M.; Beach, E. S.; Anastas, P. T.; Osuji, C. O. Smectic Demixing in the Phase Behavior and Self-Assembly of a Hydrogen-Bonded Polymer with Mesogenic Side Chains. *Macromolecules* **2010**, *43*, 6646–6654.
28. Gopinadhan, M.; Majewski, P. W.; Beach, E. S.; Osuji, C. O. Magnetic Field Alignment of a Diblock Copolymer Using a Supramolecular Route. *ACS Macro Lett.* **2012**, *1*, 184–189.
29. Majewski, P. W.; Gopinadhan, M.; Osuji, C. O. Magnetic Field Alignment of Block Copolymers and Polymer Nanocomposites: Scalable Microstructure Control in Functional Soft Materials. *J. Polym. Sci., Part B: Polym. Phys.* **2012**, *50*, 2–8.
30. Zheng, W. Y.; Hammond, P. T. Phase Behavior of New Side Chain Smectic C* Liquid Crystalline Block Copolymers. *Macromolecules* **1998**, *31*, 711–721.
31. Gopinadhan, M.; Majewski, P. W.; Choo, Y.; Osuji, C. O. Order-Disorder Transition and Alignment Dynamics of a Block Copolymer under High Magnetic Fields by *in Situ* X-Ray Scattering. *Phys. Rev. Lett.* **2013**, *110*, 078301.
32. Zakrevskyy, Y.; Faul, C. F. J.; Guan, Y.; Stumpe, J. Alignment of a Perylene-Based Ionic Self-Assembly Complex in Thermotropic and Lyotropic Liquid-Crystalline Phases. *Adv. Funct. Mater.* **2004**, *14*, 835–841.
33. Charlet, E.; Grelet, E. Anisotropic Light Absorption, Refractive Indices, and Orientational Order Parameter of Unidirectionally Aligned Columnar Liquid Crystal Films. *Phys. Rev. E* **2008**, *78*, 041707.
34. Bahadur, B. *Liquid Crystals: Applications and Uses*; World Scientific Publishing Co.: Singapore, 1990; Vol. 1.
35. Monnier, A.; Schüth, F.; Huo, Q.; Kumar, D.; Margolese, D.; Maxwell, R. S.; Stucky, G. D.; Krishnamurty, M.; Petroff, P.; Firouzi, A.; *et al.* Cooperative Formation of Inorganic-Organic Interfaces in the Synthesis of Silicate Mesostructures. *Science* **1993**, *261*, 1299–1303.
36. Zhao, D.; Feng, J.; Huo, Q.; Melosh, N.; Fredrickson, G. H.; Chmelka, B. F.; Stucky, G. D. Triblock Copolymer Syntheses of Mesoporous Silica with Periodic 50 to 300 Angstrom Pores. *Science* **1998**, *279*, 548–552.
37. Na, K.; Jo, C.; Kim, J.; Cho, K.; Jung, J.; Seo, Y.; Messinger, R. J.; Chmelka, B. F.; Ryoo, R. Directing Zeolite Structures into Hierarchically Nanoporous Architectures. *Science* **2011**, *333*, 328–332.
38. Horcas, I.; Fernández, R.; Gómez-Rodríguez, J. M.; Colchero, J.; Gómez-Herrero, J.; Baro, A. M. WSXM: A Software for Scanning Probe Microscopy and a Tool for Nanotechnology. *Rev. Sci. Instrum.* **2007**, *78*, 013705–013705−8.